A Consistent Scaling Framework for Simulating High Rate Brittle Failure Problems

Andrew L. Tonge[a], Jamie Kimberley[a], K. T. Ramesh[a]

[a] Department of Mechanical Engineering
The Johns Hopkins University
Baltimore, MD, USA

Abstract

We develop a material model that includes non-linear kinematics, a Mie-Grüneisen equation of state, and material failure based on an interacting microcrack damage model. This material model is well suited for simulating hypervelocity impacts on brittle materials. By accounting for the subscale distribution of cracks within the material, we are able to produce a material model that does not require assumptions about how material strength scales with specimen size. This allows us to calibrate the model at laboratory scales and then apply the model under conditions that are not achievable in a laboratory setting such as asteroid impacts.

© 2013 The Authors. Published by Elsevier Ltd. Open access under CC BY-NC-ND license.

Selection and peer-review under responsibility of the Hypervelocity Impact Society

1. Introduction

Predictive modeling of hypervelocity impact events involving brittle materials is important for fields as diverse as armor ceramics (Department of Defense), infrastructure security (Department of Homeland Security), and planetary science (NASA). Since impact events involve the interaction of complex geometries with dynamic loading, numerical simulations of the impact events are often necessary. The strength of brittle materials can depend on the loading rate, loading history, and sample volume. One common approach addressing these dependencies is to develop a heuristic damage model which can be fit to experiments. A commonly used example of a heuristic damage model is the JH2 model by Johnson and Holmquist [1]. These heuristic damage models have parameters that account for history, rate, and size effects, which makes them very powerful when the model parameters can be fit using experiments.

Problems begin to arrise when these heuristic models are used to predict the outcome of impact events that occur outside of the range of experimental conditions that were used for calibration. Since these models lack well defined scaling physics, it is difficult to determine the limits for applicability of a given material model and how the accuracy of that model degrades as that limit is approached. This issue is particularly apparent for asteroid impact simulations because it is not possible to perform calibration experiments that are on the size scale of asteroid impacts. In this work we develop a mechanism-based damage model to help address the issue of extending experimental results up to scales which are several orders of magnitude different in size. Since a mechanism-based damage model introduces additional physics into the failure model, it can take advantage of observations that are not available to other types of damage models and eliminate scale dependent parameters which require experimental calibration. We develop a model based on the work of Paliwal and Ramesh [2] and then test the model by comparing simulation results to impact experiments where the development of damage was recorded with microsecond resolution [3].

This paper is organized as follows. The constitutive model is presented for a general material. Once the model has been presented the simulation and experiment are described and the model parameters are discussed. Finally, the results of the simulation are presented followed by a discussion of the results.

Email address: andy.tonge@jhu.edu (Andrew L. Tonge)

2. Constitutive Model

2.1. Model Framework

The deformation gradient $F = \frac{\partial x}{\partial X}$ transforms an infinitesimal line segment dX in the reference configuration into an infinitesimal line segment in the deformed configuration dx. The balance of linear momentum is written in the deformed configuration using the Cauchy stress σ. The stress can be separated into a deviatoric portion S and a hydrostatic (pressure) portion $P = -\frac{1}{3}\mathrm{tr}(\sigma)$ using the relationship $S = \sigma + PI$. Here I is the second order identity tensor. We relate the deviatoric portion of the stress linearly to the deviatoric part of the finger tensor ($b = FF^T$) using the shear modulus G, so that $S = G\left(b - \frac{1}{3}\mathrm{tr}(b)\,I\right)$.

The pressure is computed using the Mie-Grüneisen equation of state ($P - P_H = \Gamma\rho(E - E_H)$). Where P, E, and ρ are the pressure, internal energy per unit mass, and density at the current state. P_H and E_H are the pressure and internal energy obtained from the Hugoniot at the density ρ. Additionally we follow equation 5.18 in Meyers [4] and assume that the Grüneisen parameter Γ is a function of the material density such that $\Gamma\rho = \Gamma_0\rho_0$. Here Γ_0 and ρ_0 are the Grüneisen parameter and material density at room temperature and pressure. Following the standard arguments to compute the pressure and energy on the Hugoniot as presented by Meyers [4] and assuming a linear relationship between the shock speed U_s and the particle velocity U_p ($U_s = C_0 + S\,U_p$) we can relate the pressure to the internal energy per unit mass E, initial density ρ_0, and volumetric strain ($\eta = 1 - \det(F)$) using

$$P = \Gamma_0\rho_0 E + \frac{C_0^2\eta\rho_0\left(1 - \frac{\Gamma_0}{2}\right)}{(1 - S\eta)^2}. \tag{1}$$

At small volumetric strains, this relationship recovers a linear relationship between the pressure and the volumetric strain, but as the material is compressed the response stiffens which leads to the formation of shocks.

2.2. Dynamics

As discussed in section 2.1 the balance of linear momentum is written in the deformed configuration where the material derivative of the velocity multiplied by the density is equal to the divergence of the Cauchy stress ($\rho\dot{v} = \nabla\cdot\sigma$). Angular momentum is satisfied by requiring a symmetric stress tensor. In the short times associated with impact events, we assume that heat transfer is negligible. As a result, the rate of mechanical work done per unit mass is equal to the change in internal energy per unit mass ($\dot{E} = \frac{1}{\rho}\sigma : d$). Here d is the rate of deformation tensor. We assume that the internal energy per unit mass is composed of a strain energy density e_s and a thermal energy per unit mass $E_\theta = c_v\theta$. Here c_v is the specific heat and θ is the temperature. The elastic strain energy density is equal to the difference between the total internal energy per unit mass and the thermal energy per unit mass ($e_s = \rho(E - E_\theta)$). Since we are not considering thermal conduction, changes in temperature are due entirely to shock heating. The heating rate due to shock heating depends on the temperature, density, and rate of compression

$$\dot{\theta} = \frac{-\theta\Gamma\rho_0}{\rho}\mathrm{tr}(d). \tag{2}$$

2.3. Micromechanics Damage model

Up to this point, we have presented a constitutive model which assumed a homogeneous material where the dissipative mechanism is shock heating. In addition we model internal damage growth by degrading the stress response of the material which results in an additional dissipation mechanism. The damage model we use captures the interaction and growth of cracks at a scale finer than the computational mesh.

We quantify the level of subscale damage using a scalar damage variable based on the amount of crack growth

$$D = \sum_{k}^{N_f} \omega_k l_k^3. \tag{3}$$

The damage contribution of a family of flaws is the length that a single flaw in that family has grown l_k, cubed for dimensional consistency, multiplied by the number density (units of m^{-3}) of the flaws in that family ω_k. This damage definition lets us incorporate a distribution of flaws by discretizing the probability density function of the flaws such that $\omega_k = \eta g(s)_k\Delta s$. Here η is the average flaw density and $g(s)$ is the probability density function (PDF) that describes the likelihood that a given flaw has size s.

2.3.1. The Effect of Damage

To represent the effect of damage on the material, we degrade the pressure response $P(E, \rho) = \kappa_p P_0(E, \rho)$ and the shear modulus $G = \kappa_G G_0$ of the material. P_0 and G_0 are the undamaged pressure and shear modulus of the material while P and G are the damaged pressure and shear modulus. The coefficients κ_p and κ_G carry the effect of the damage and are defined below.

For the shear response we use the basic form proposed by Budiansky and O'Connell [5], but add the simplifying assumption that the prefactor κ_G depends only on the initial Poisson's ratio and the current damage level

$$\kappa_G = 1 - \frac{32}{45}\left(\frac{(1-\nu_0)(5-\nu_0)}{2-\nu_0}\right)D. \tag{4}$$

For the pressure response, we start with the relationship that was presented in Budiansky and O'Connell [5] and then assume that the damage effect depends only on the initial Poisson's ratio and the current damage level

$$\kappa^* = 1 - \frac{16}{9}\left(\frac{1-\nu_0^2}{1-2\nu_0}\right)D. \tag{5}$$

To complete the definition of κ_p we account for a different damage effect in compression and in tension. We motivate this asymmetry using sand as an example of a fully damaged material. Although the sand has no resistance to hydrostatic tension, it can support significant hydrostatic compression. We account for this asymmetry by limiting the damage effect on the pressure (κ_p) when the material is under compressive load using the parameter κ_1 which we choose to be 0.5, so that,

$$\kappa_p = \begin{cases} \kappa_1 & P_0 > 0 \text{ and } \kappa^* < \kappa_1 \\ \kappa^* & \text{otherwise} \end{cases}. \tag{6}$$

The parameter κ_1 can be interpreted as the ratio between the bulk modulus of the damaged material and the bulk modulus of the intact or undamaged material.

2.3.2. Damage Evolution Model

For this work we start from the damage model developed by Paliwal and Ramesh which is particularly effective for calculating the peak strength of the material under uniaxial compression loading [2]. We add necessary assumptions to extend the model to general three dimensional stress states and a non-linear elastic material response. They developed a micromechanics damage model which incorporates a distribution of flaws within the material and accounts for crack interactions using the self consistent method. In the self consistent method, each crack is surrounded by an ellipse which contains only undamaged material. The matrix that contains the ellipse is the homogenized material. In the model developed by Paliwal and Ramesh [2] the matrix was an orthotropic material with an elastic stiffness based on the softening model in Budiansky and O'Connell [5]. In order to extend the application of the self consistent method to a material with a non-linear elastic response we assume an isotropic matrix and use tangent modulus of the material which was discussed in the previous sections. The matrix and inclusion problem relates the applied stress, the current damage state and the local stress around the crack σ^e consistently which accounts for crack interactions at the microscale.

The driving force for crack growth K_I depends on the stress in the ellipse σ^e, the initial flaw size s, the angle between the flaw normal and the compressive loading direction ϕ, the coefficient of friction between the crack faces μ, and the wing crack length l

$$K_I = \frac{F_w}{\sqrt{\pi(l + 0.27s)}} + \sigma_{22}^e \sqrt{\pi(l + \sin(\phi)s)}. \tag{7}$$

Here the wedging force F_w represents the opening force on the crack due to crack face sliding. It arises because the contacting crack faces can transmit the full normal component of the traction acting across the crack faces but not the full shear component. The mismatch can be interpreted as an extra force that opens the wing cracks.

To compute the crack growth rate $\dot{l}$ we adopt the Freund crack growth law [6]

$$\dot{l} = \frac{C_r}{\alpha_c}\left(\frac{K_I - K_{IC}}{K_I - 0.5K_{IC}}\right)^{\gamma_c}. \tag{8}$$

Here C_r is the Rayleigh wave speed, and α_c and γ_c are dimensionless constants determined experimentally by measuring the crack velocity as a function of the applied stress intensity factor.

2.3.3. Damage Model Extension to General Loading

To extend the model from two dimensions to an arbitrary three-dimensional stress state encountered in a three-dimensional simulation, we introduce additional assumptions. Instead of tracking the orientation of flaws in three dimensions, we select an equivalent two-dimensional stress state which maximizes K_I. We select the plane that contains the direction of the maximum (most tensile) principal stress and the minimum (most compressive) principal stress. We then define the orientation of the flaw by measuring ϕ from the minimum principal stress. Under these conditions both the wedging force (F_w) and the direct contribution (σ_{22}^e) to the stress intensity factor are maximized. This approximation discards the middle principal stress because it is out of plane and does not contribute to the mode-I stress intensity factor. Experimental studies on metals have show that materials tend to have a greater resistance to fracture under plane stress conditions than under plane strain conditions, but this difference is a difference in the effective fracture toughness not in the applied stress intensity factor. Since fracture toughness is measured under plane strain conditions by convention, we assume that there is a single mode-I

fracture toughness for the material of interest and use that value. With the introduction of these assumptions, the model can address crack growth under multi-axial compression when the wing cracking mechanism is active.

In addition to a three dimensional stress state, we must address the case where crack faces may separate and lead to pure tensile crack growth. To address this loading condition, we limit the wedging force to be non-negative ($F_w \geq 0$). As a result of this limitation we recover $K_I = \sigma_{22}^e \sqrt{\pi(l + \sin(\phi)s)}$ under appropriate conditions. This is consistent with the stress intensity factor for a crack in a large plate under tension.

The self consistent method is well suited to capture crack interactions for low to moderate damage levels, however in the impact problem there are regions where the material becomes fully damaged. To bridge the gap between the moderate damage regime, where the self consistent model is reasonable, and the fully damaged state of the material we introduce a critical damage level D_c. When the damage level exceeds D_c cracks that have grown more than 0.1 percent of their initial size continue to grow, but all other cracks stop growing. For cracks that continue to grow we assume that interactions cause them to grow at the limiting crack velocity of $\frac{C_r}{\alpha_c}$. As a result, damage continues to grow rapidly until the material point is completely failed. We define a material point as completely failed when either of the prefactors that effect the stress (κ_p or κ_G) drop below a critical value κ_2. When this occurs we tag the particle as failed and it cannot sustain either tensile or shear stresses

$$\sigma = \begin{cases} -\kappa_p P_0 \boldsymbol{I} & P_0 > 0 \\ \boldsymbol{0} & \text{otherwise} \end{cases} . \tag{9}$$

This physically based micromechanics damage model can be used to simulate the failure of brittle materials subjected to arbitrary loading histories. All of the parameters for the model except for the flaw distribution can be obtained from laboratory scale experiments. The Mie-Grüneisen equation of state required the relationship between shock speed and particle velocity which can be obtained using plate impact experiments. The specific heat c_v, density ρ, shear modulus G, and fracture toughness K_{IC} can all be obtained using standardized testing procedures. Our model assumes that these are independent of the scale of the simulation. Scale effects are introduced by the flaw density η and the probability density function for the flaw size $g(s)$. These quantities can be estimated based on surface observations following the method presented by Piggot [7] which should enable predictive simulations of asteroid impacts.

2.4. Thermodynamic Framework

This material model incorporates the effects of recoverable elastic deformation, internal damage growth, and temperature which must be consistent with the second law of thermodynamics. By applying the thermodynamic framework in Clayton [8] to the material model discussed in the preceding subsections, we can reduce the standard argument by Coleman and Gurtin [9] to an inequality which requires that the energy dissipated by the internal damage variable is non-negative

$$-\frac{\partial \Psi}{\partial D}\dot{D} \geq 0. \tag{10}$$

Here Ψ is the free energy per unit mass and D is the internal variable that tracks damage. Since an increase in the damage variable leads to a reduction in the elastic modulus ($\frac{\partial \Psi}{\partial D} < 0$), equation (10) is satisfied by construction because $\dot{D} \geq 0$.

3. Simulation Setup

To test the capabilities of the material model presented in Section 2, we simulated high velocity impact experiments where the damage history was recorded in real time [3]. The experiments consisted of a target cube 100 mm on a side which was constructed by bonding a half cube of Pyrex to a half cube of basalt. The cube was impacted by a Pyrex sphere 6.5 mm in diameter at a velocities of 1.0 and 2.0 km/s. Using high speed imaging, the failure process was captured by looking through the glass as the basalt failed. The experimental setup is shown in Fig. 1. We compare the imaging data to the damage history of the simulation to assess the capability of the material model.

3.1. Computational Framework

The simulations were conducted using the Generalized Interpolation Material Point Method (GIMP) [10] which has been implemented in the Uintah computational framework [11]. GIMP is a quasi-meshless method which evolved from the particle in cell technique. The basic concept is that Lagrangian material points carry the history information for each material point. This history information is used to compute the stress at the material point. After computing the stress at the material point this stress is projected onto a background mesh where the equations of motion are solved. The regular background mesh improves the accuracy and simplicity of calculating gradients while the Lagrangian material points provide accurate tracking of history variables. Since the material points can convect through the Eulerian background, GIMP avoids mesh distortion issues that can arrise with traditional Finite Element type approaches. For these simulations we selected a grid spacing of 1 mm per cell and 8 particles per cell based on the available computational resources.
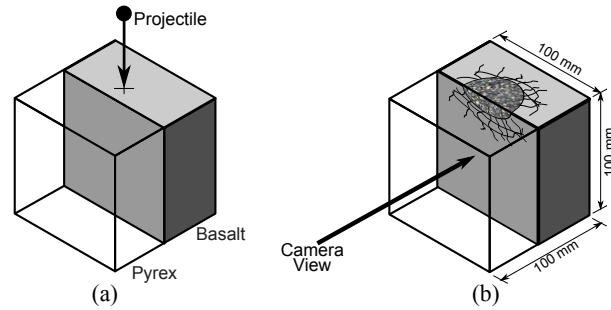
Fig. 1: Schematic of experimental setup for visualizing damage growth during high velocity impact experiments on basalt bonded to Pyrex. Prior to impact (a) and after impact (b).

Table 1: Material model parameters for Pyrex and basalt

Property	Units	Basalt	Pyrex
Density (ρ_0)	kg m^{-3}	2,874	2,230
Specific Heat Capacity (c_v)	(J K^{-1} kg^{-1})	840	750
Shear Modulus (G)	GPa	29.0	27.0
C_0	ms^{-1}	4,200	4,564
S		0.71	1.73
Γ		0.42	0.53
Fracture Toughness (K_{IC})	MPa $\sqrt{m}$	1.6	0.78
Coefficient of Friction (μ)		0.57	0.4
Flaw Angle (ϕ)	Radians	1.0444	0.9757
γ_c		1.0	1.0
α_c		5.0	1.0
Minimum Flaw Size (s_{min})	μm	1.0	1.0
Maximum Flaw Size (s_{min})	μm	1,000	75
Power-law Exponent (α)		4.5	3.0
Flaw Density (η)	m^{-3}	3×10^{17}	5×10^{12}
Critical Damage (D_c)		0.1	0.1
κ_1		0.5	0.5
κ_2		0.001	0.001

3.2. Model Parameter Estimation

The material model that we presented in section 2 contains numerous parameters that must be estimated prior to performing a simulation. For discussion we break these parameters into three groups. First there are parameters that relate the to bulk thermoelastic response of the material. These include the equation of state parameters (S, Γ_0, and C_0), the reference density (ρ_0), the specific heat capacity (c_v), and the shear modulus (G). All of these quantities are readily obtained from literature or standard experimental techniques. The second group of material parameters are related to the internal flaw distribution in the material (η and $g(s)$). In principal it should be possible to measure the distribution of flaws in a laboratory scale specimen given sufficient funds and time. However, in practice the techniques that are used to determine the flaw distribution destroy the specimen and are time consuming so a complete catalogue of the internal flaws in the specimen is not available. The third group of material parameters are related to the growth of microcracks within the material. These parameters include the fracture toughness (K_{IC}), internal coefficient of friction (μ), the crack angle (ϕ), and the parameters specific to damage accounting in this model (D_c, κ_1, and κ_2).

For Pyrex (borosilicate glass) we used equation of state parameters found in Forde et al. [12]. For the basalt we used the low density parameters found in Ahrens and Johnson [13]. Since the Grüneisen parameter was not reported in this work, it was estimated based on $\Gamma_0 = 2S - 1$ from Meyers [4].

As discussed earlier, we specify that the maximum degradation of the pressure response of the material is 50 percent of its undamaged value ($\kappa_1 = 0.5$). This value could be further constrained by measuring the ratio of the bulk modulus for the fully damaged material to the bulk modulus of the intact material. After fixing the maximum degradation of the bulk modulus in compression, we set the critical damage level for continued crack growth (D_c) to ensure that unstable crack growth occurs before the limiting bulk modulus value is reached. Solving equation (5) with $\kappa^* = \kappa_1$ for damage parameter D gives the maximum damage level before our choice of κ_1 can effect the pressure response. For the Basalt this occurs at $D = 0.145$ and for the Pyrex this occurs at $D = 0.147$. We select the damage threshold $D_c = 0.1$ which is below this level to insure that unstable crack growth occurs before the pressure response is affected by κ_1. This damage threshold may seem low when considered on the common 0 to 1 damage scale, however for the softening model that we have chosen,

the damage required to drive the bulk modulus to 0 is between 0.28 and 0.30 for the basalt and Pyrex. Additionally, we recognize that once a material point has started to soften, the macroscopic interactions of that material point with the neighborhood around the point should cause rapid localization and failure of the material point. We select the threshold for tagging particles as localized (κ_2) and unable to sustain shear stresses to be a small value which is well after the peak stress is obtained. For these simulations this value was set to $\kappa_2 = 0.001$.

The remaining quantities of fracture toughness (K_{IC}), the internal coefficient of friction (μ), the crack angle (ϕ), and the flaw distribution (η, and $g(s)$) all contribute to the measured strength of the material. For the Pyrex we selected a fracture toughness of 0.78 MPa $\sqrt{m}$ based on similar borosilicate glasses that were tested by Weber et al. [14]. We selected the internal coefficient of friction for the glass as 0.4. From the coefficient of friction we can use follow [15] and compute the most damaging flaw angle as $\phi = \frac{\pi}{2} - \frac{1}{2}\tan^{-1}(\frac{1}{\mu})$. For basalt the coefficient of friction was calculated based on a friction angle of 30°. This gives an internal coefficient of friction (μ) of 0.57 and a most damaging flaw angle of $\phi = \frac{\pi}{3}$. The fracture toughness for basalt is not as well constrained as that of the borosilicate glass. Balme et al. [16] found fracture toughnesses for different types of basalts or solidified lava flows from 1.29 MPa $\sqrt{m}$ to 2.8 MPa $\sqrt{m}$ or higher depending on the amount of confinement or the heat treatment prior to testing. Without performing fracture toughness testing on the specific basalt specimen that we used for our experiments we must select some combination of flaw distribution and fracture toughness that gives a quasistatic strength in the range that was experimentally observed. For the basalt in this work we selected a fracture toughness of 1.6 MPa $\sqrt{m}$.

As discussed in Housen and Holsapple [17] the distribution of cracks in geologic materials tend to follow a power-law type distribution. As discussed in the description of the model we describe the subscale flaw distribution using a flaw density η and a probability density function for the flaw size $g(s)$. For the flaw size probability density function $g(s)$, we use a bounded Pareto distribution

$$g(s) = \begin{cases} \frac{\alpha s_{min}^{\alpha} s^{-(\alpha+1)}}{1 - \left(\frac{s_{min}}{s_{max}}\right)^{\alpha}} & s_{min} < s < s_{max} \\ 0 & \text{otherwise} \end{cases} . \tag{11}$$

This distribution can be considered a subset of the full power-law distribution discussed by Housen and Holsapple [17] and Piggot [7]. In those studies they measured flaw sizes over many orders of magnitude they determined that for most geologic materials the flaw size distribution followed a power-law with an exponent (α) between 3 and 6. The power-law distribution described by Piggot [7] and measured by Housen and Holsapple [17] for granite is valid for a very large range of scales. To simulate the result of the impact event we must introduce a numerical discretization into the problem. This discretization adds a length scale to the problem and divides the power-law distribution into two portions. One portion is the part of the distribution that represents flaws that are larger than the mesh size while the rest of the distribution is smaller than the mesh size. Since the material model describes the evolution of subscale flaws, we set the upper cutoff for the flaw size in the basalt as 1 mm. For a true power-law distribution there is no lower limit on the flaw size. However, this does not make physical sense because, at some point the microstructure of the material will become important and that will disrupt the power law nature of the flaw distribution. However, for materials where the microstructural size is much smaller than the numerical resolution it makes sense to assume a power-law behavior for the subscale distribution. From a computational point of view, we need to introduce a minimum flaw size inorder to discretize the distribution. Additionally, the cost of integrating the constitutive equations will scale with the number of bins used to discretize the distribution. So for a fixed cost, a narrower distribution can be discretized more accurately. To insure that the minimum flaw size is sufficiently small that we are approximating a distribution without a cutoff for small flaw sizes we check the length of the wing cracks that have grown from the smallest flaw. Ideally there would be no particles that show additional crack growth for the smallest bin of flaws. For our simulations a small number of particles near the impact site exhibited limited crack growth in their smallest bin, however we feel that this represents a reasonable balance between capturing the ideal behavior of an unbounded power-law distribution of flaws and the computational expense of accounting for many families of flaws that may not get activated.

A similar argument holds for the flaw sizes in the Pyrex. Volumetric flaws in the Pyrex are a result of the processing history and are likely to be very small. Since the Pyrex is optically transparent and there were no visible flaws in the pieces that were used, we assume that the maximum flaw size in the material is 75 μm, which is a reasonable detection limit for the unaided human eye. A power-law type flaw distribution in the Pyrex is reasonable because durring cooling when a crack is initiated, it is likely that the crack draws its energy from an area around it which scales with the size of the crack. To obtain a self similar flaw spacing where the average flaw spacing for flaws greater than a size s scales linearly with the flaw size, the exponent for the distribution must be 3.0. This argument is discussed in more detail in Housen and Holsapple [17].

The crack growth parameters α_c and γ_c can be determined by observing a single crack propagating under known conditions. The exponent that characterizes the sensitivity of the crack velocity to the stress intensity factor (γ_c) is very difficult to measure experimentally since it requires measuring the crack velocity as a function of the applied stress intensity factor. For the purposes of this set of simulations we use $\gamma_c = 1.0$ for both the Basalt and the Pyrex. The limiting crack growth speed can be estimated from high speed imaging during dynamic testing. For Basalt the maximum observed crack speed was between 200 m/s and 500 m/s. In basalt the Rayleigh wave speed is 2,920 m/s so a value of $\alpha_c = 5$ is reasonable based on experimental evidence. Cracks propagating in the Pyrex will not be deflected by grain boundaries or other sub scale features so they should move faster than the cracks in the Basalt. Additionally a smaller value of α_c results in faster cracks which contributes to lower rate sensitivity which is expected based on experiments which were conducted on single crystal Quartz. For the Pyrex we selected $\alpha_c = 1.0$.

The remaining parameter that contributes to the strength of the material is the flaw density (η). Under compression even at low rates the strength is sensitive to the flaw density since cracks grow stably. To determine the flaw density, we performed single particle simulations
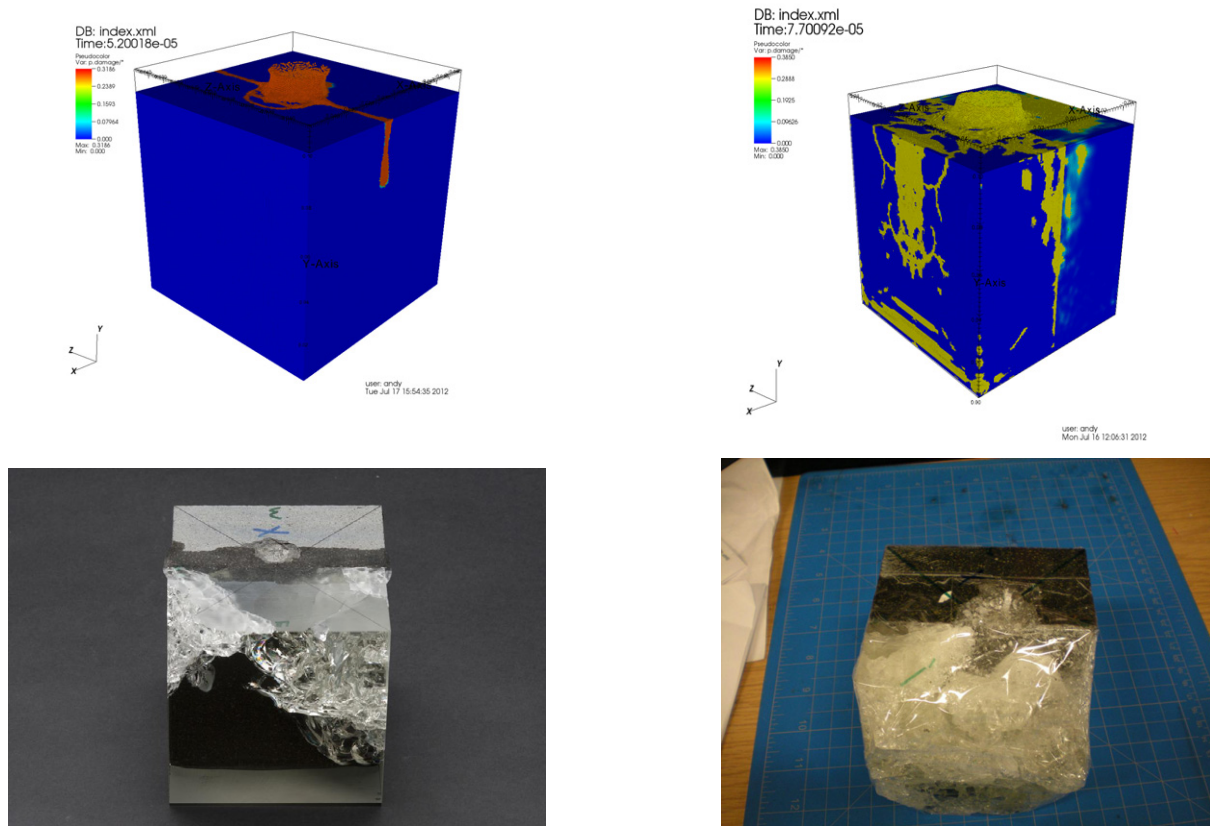
Fig. 2: Comparison of final damage state for simulations and experiments at 1.0 km/s and 2.2 km/s.

where the stress state is homogenous uniaxial stress and fit the quasi-static strength of the material. After fitting the quasistatic strength we run simulations at strain rates of 10^3 s^{-1} and 10^4 s^{-1} to make sure that the rate sensitivity of the material is reasonable. For basalt the quasistatic compressive strength is 450 MPa while the quasistatic compressive strength for Pyrex is 1 GPa. We expect much greater rate sensitivity from the basalt than the Pyrex. Using this procedure we obtained a flaw density of 3×10^{17} m^{-3} for the basalt and 5×10^{12} m^{-3} for the Pyrex. The material model parameters for the Basalt and the Pyrex are summarized in table 1.

4. Simulation Results

We look at four different metrics for comparing the simulation results to the experimental visualization of the failure process. The easiest experimental quantity to measure is the final crater size. A second measure that is related to the crater size is the final distribution of damage. In addition to these two post mortem quantities we look at the velocity of the damage front and the features that develop in the damage zone.

For the impact at 1.0 km/s the crater depth at the end of the simulation (52 μs) was 8 mm with a diameter of 21 mm. This compares to a crater depth of 3.9 mm and diameter of 20 mm in the experiments. When the impact velocity is increased to 2.2 km/s the simulated crater depth increased to 21 mm while the diameter increased to 29 mm at 77 μs. The experimental crater depth was 9.0 mm with a crater diameter of 33 mm for an impact velocity of 2.2 km/s.

The final damage distributions for the 1.0 and 2.2 km/s impact velocities are shown in figure 2. On the left is the 1.0 km/s impact while the right has the 2.2 km/s impact. The simulation results are on the top showing a plot colored according to damage. Hotter colors (yellow orange and red) indicate damaged material while blue indicates undamaged material. The 1 km/s simulations show a large damaged region near the impact site with a damage region extending along the glass-basalt interface. There is some localization of the damage region towards its outer limits. The simulations indicate that the glass should remain mostly intact, but probably split from the basalt. The postmortem image from the experiment indicates that there is a small amount of damage at the impact site, the basalt remains bonded to the glass, and there are free surface effects at the corners of the glass which cause significant amounts of damage.
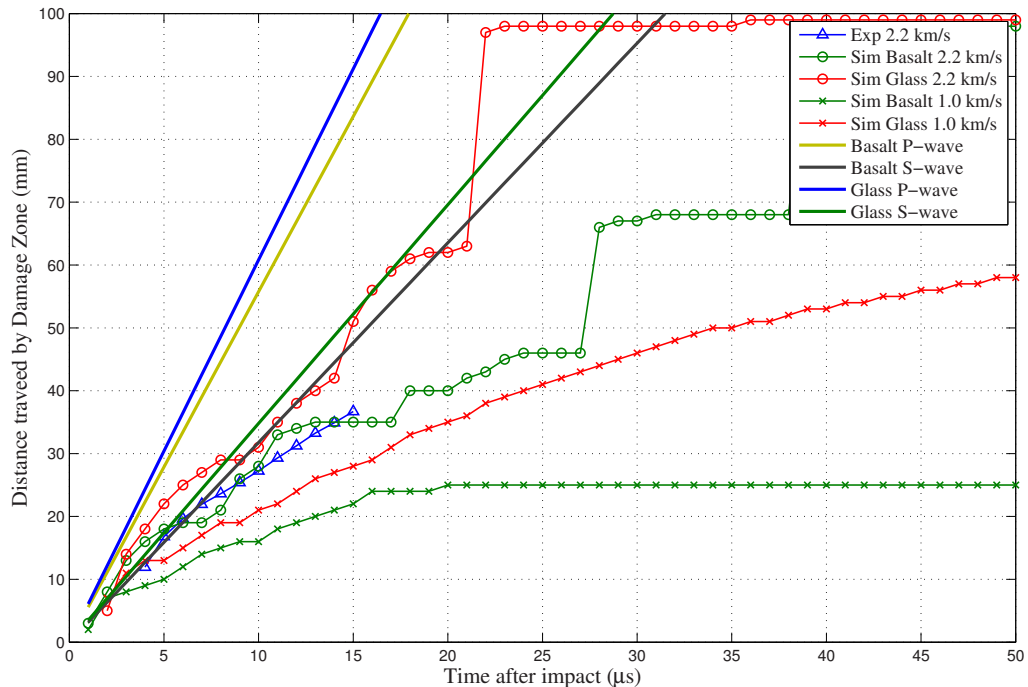
Fig. 3: Comparison of damage zone extend from impact site as a function of time for the 2.2 km/s experiment, and the simulations at 1.0 km/s and 2.2 km/s. The experimental data is calculated by looking through the glass at the propagation of the damage zone and the simulation data is determined by looking either at only the basalt (Sim Basalt) or the glass (Sim Glass). The P-wave and S-wave locations are also drawn in for reference.

For the 2.2 km/s impact velocity the is significantly more damage. The simulations suggest that the glass is almost completely fragmented, while there is significant damage to the basalt. The preferred locations for damage growth are along the glass-basalt interface, and in planes parellel to the surfaces of the cube. The damage growth history suggests that the damage initially grows from the impact site in a radially expanding damage zone. The damage then transitions to growing preferentially along the basalt-glass interface like in the 1.0 km/s impact. However since there is a much larger amount of energy present in the 2.2 km/s impact there is sufficient energy in the wave reflected from the sides of the cube to cause spall in the glass. The experimental observations show significant damage in the glass especially at late stages when free surface interactions are likely. The postmortem picture of the 2.2 km/s impact shows a large amount of damage in the glass and some damage in the basalt, however since the basalt is not transparent it is difficult to determine the exact amount of damage that is present in the basalt.

From the simulations we can extract two different damage zone velocities. First is the damage zone in the glass. This is the largest damage zone and it moves faster than the damage zone in the basalt. Figure 3 shows the damage zone position history as a function of time for the basalt and glass in each of the simulations as well as the position history of the damage zone in the 2.2 km/s experiment. We were not able to extract the damage zone position history fro the 1.0 km/s impact. There is reasonable agreement between the damage zone in the basalt for the 2.2 km/s impact and the experimental observation of the damage zone location. At early times for the 2.2 km/s impact the damage zone travels faster than the shear wave speed in either the basalt or the glass. This suggests that we are capturing a mechanism that allows damage growth under high confinement. The large jump in the damage zone position is he result of spall at the back surface.

5. Discussion

The simulations were able to capture the development and growth of damage in both the glass and the basalt using a material model that is valid across many length scales. Important features of the impact event that the model captured include the growth of damage under primarily compressive states and the structural interactions between the loading and the glass-basalt interface and the loading waves with the free surface. The model has difficulty capturing the correct crater shape and at the higher impact velocity there is more damage in the simulation that we observe in the experiments.

We believe that the model predicts excessive damage for the 2.2 km/s impact velocity because the model does not incorporate enough of the relevant physics and provide sufficient energy dissipation pathways. The material model that is presented in this paper does not address the granular flow of the material after it has been fully damaged. Providing this additional energy dissipation pathway should limit the final crater size and may reduce the total amount of damage present at the end of the simulation. Additionally, in the experiments the impact site was offset into the basalt, while in the simulations the impact was centered on the glass-basalt interface. It is possible that by impacting the basalt more of the impact energy was trapped in the basalt which is stronger than the glass at high rates. There are also minor differences in the boundary conditions on the face opposite the impact site. In the experiments this face was resting on the support table, while in the simulations the target cube is floating in space. The contact with the support table provides an additional energy path which should further reduce the amount of damage in the specimen. Contact with the table should suppress spall parallel to the bottom suface of the specimen.

We plan to continue developing this material model in order to better capture the relavent physics in the problem. We are working on incorporating granular flow of the damaged material which would replace the assumption that the fully damaged material can sustain no deviatoric stresses. By incorporating this additional physical mechanism we expect to improved the models ability to model the post damage flow of the material which is important for cratering or penetration problems. The high confinement in these types of problems should give the damaged material significant shear strength. Additionally, we plan to adapt the model so each material point represents a realization of the subscale flaw distribution. This will result in each material point having a slightly different failure strength and rate sensitivity. As discussed by Brannon et al. [18] and Daphalapurkar et al. [19], this macroscopic variability should help mitigate mesh sensitivity issues which are commonly associated with material models that contain a softening stress strain response and will be based on a physically reasonable principal.

Overall we feel that this damage model provides a reasonable approach to simulating the massive failure that results from hypervelocity impact events. As we discussed in section 3.2 we are able to constrain most of the model parameters based on literature values and a few calibration tests. In the simulations that we presented the parameters that were most difficult to constrain were the fracture toughness, the non-dimensional parameters in the crack growth law, and the flaw distribution. This represents an important step towards developing a material model that can be validated at laboratory scales and then extended to asteroid scales.

6. Conclusion

We developed and implemented a micromechanics based material model that is appropriate for brittle failure under high loading rates. This material model accounts for rate and size effects by explicitly simulating the evolution of an ensemble of sub-scale flaws. This flaw distribution can be calibrated either through surface observations or by fitting experimental data. All of the other parameters for the model are assumed to be scale independent. This results in a model that is ideal for simulating large scale impacts in size and velocity ranges where experiments are either difficult, costly, or not feasible. This type of model should find applications from armor ceramics to asteroid impacts.

References

[1] G. R. Johnson, T. J. Holmquist, An improved computatonal constitutive model for brittle materials, High Pressure Science and Technology (1993) 981–984.
[2] B. Paliwal, K. Ramesh, An interacting micro-crack damage model for failure of brittle materials under compression, Journal of the Mechanics and Physics of Solids 56 (2008) 896–923.
[3] J. Kimberley, K. Ramesh, Visualization of early stage damage propagation during hypervelocity impacts on brittle materials, This Procedings (2012).
[4] M. A. Meyers, Dynamic Behavior of Materials, John Wiley & Sons, inc, 1994.
[5] B. Budiansky, R. J. O'Connell, Elastic moduli of a cracked solid, International Journal of Solids and Structures 12 (1976) 81 – 97.
[6] L. Freund, Crack propagation in an elastic solid subjected to general loading-ii. non-uniform rate of extension, Journal of the Mechanics and Physics of Solids 20 (1972) 141–152.
[7] A. R. Piggot, Fractal relations for the diameter and trace length of disk-shaped fractures, Journal of Geophysical Research 102 (1997) 18,121–18,125.
[8] J. D. Clayton, Deformation, fracture, and fragmentation in brittle geologic solids, International Journal of Fracture 163 (2010) 151–172. Cited By (since 1996): 1.
[9] B. Coleman, M. Gurtin, Thermodynamics with internal state variables, Journal of Chemical Physics 17 (1967) 597–613.
[10] S. Bardenhagen, E. Kober, The generalized interpolation material point method, CMES - Computer Modeling in Engineering and Sciences 5 (2004) 477–495.
[11] S. Parker, J. D. de St. Germain, J. Schmidt, T. Harman, J. Guilkey, M. Others, Uintah Website, 2011. Http://www.uintah.utah.edu.
[12] L. Forde, W. Proud, S. Wally, P. Church, I. Cullis, Ballistic impact studies of a borocilicate glass, International Journal of Impact Engineering (2010).
[13] T. J. Ahrens, M. L. Johnson, Shock wave data for rocks, Rock Physics and Phase Relations (1995).
[14] W. Weber, H. Matzke, J. Routbort, Indentation testing of nuclear-wast glasses, Journal of Materials Science (1984) 2533–2545.
[15] M. F. Ashby, S. D. Hallam (Ne Cooksley), The failure of brittle solids containing small cracks under compressive stress states, Acta Metallurgica 34 (1986) 497–510.

[16] M. Balme, V. Rocchi, C. Jones, P. Sammonds, P. Meredith, S. Boon, Fracture toughness measurements on igneous rocks using a high pressure, high temperature rock fracture mechaincs cell, Journal of Volcanology and Geothernal Research 132 (2004) 159–172.

[17] K. R. Housen, K. A. Holsapple, Scale effects in strength-dominated collisions of rocky asteroids, Icarus 142 (1999) 21 – 33.

[18] R. Brannon, J. Wells, O. Strack, Validating theories for brittle damage, Metallurgical and Materials Transactions A: Physical Metallurgy and Materials Science 38 A (2007) 2861–2868.

[19] N. P. Daphalapurkar, K. T. Ramesh, L. Graham-Brady, J. F. Molinari, Predicting variability in the dynamic failure strength of brittle materials considering pre-existing flaws, Journal of the Mechanics and Physics of Solids 59 (2011) 297–319.